Research Article | Vol. 9, No. 8 / 1 August 2019 / Optical Materials Express 3352
Optical Materials EXPRESS

Temperature dependence of Alexandrite effective emission cross section and small signal gain over the 25-450 °C range

UMIT DEMIRBAS,[1,2,*] ALPHAN SENNAROGLU,[3,4] AND FRANZ X. KÄRTNER[1,5]

[1] *Center for Free-Electron Laser Science, Deutsches Elektronen-Synchrotron DESY, Luruper Chaussee 149, 22761 Hamburg, Germany*
[2] *Laser Technology Laboratory, Antalya Bilim University, 07190 Dosemealti, Antalya, Turkey*
[3] *Koç University Surface Science and Technology Center, Rumelifeneri, Istanbul 34450, Turkey*
[4] *Laser Research Laboratory, Departments of Physics and Electrical-Electronics Engineering, Koç University, Istanbul 34450, Turkey*
[5] *Physics Department and The Hamburg Centre for Ultrafast Imaging, University of Hamburg, Luruper Chaussee 149, 22761 Hamburg, Germany*
[*] *uemit.demirbas@cfel.de*

Abstract: We present detailed measurements of effective emission cross section spectra of the Alexandrite gain medium in the 25-450 °C temperature range and provide analytic formulas that can be used to match the measured spectra. The measurement results have been used to investigate the wavelength and temperature dependence of small signal gain, as well as gain bandwidth relevant for ultrafast pulse generation/amplification. We show that the estimated laser performance based on the measured spectroscopic data provides a good fit to the results in the literature. We further discuss the need for a detailed measurement of excited-state absorption cross section in future studies.

© 2019 Optical Society of America under the terms of the OSA Open Access Publishing Agreement

1. Introduction

Alexandrite (chromium-doped chrysoberyl, Cr^{3+}:$BeAl_2O_4$) laser crystals possess a broad emission band centered around 750 nm that enables tunable laser operation in the 700-860 nm wavelength range [1–5]. Moreover, it has extensive absorption bands in the visible region of the optical spectrum, which facilitate efficient pumping either by flahslamps or by red laser diodes. Furthermore, Alexandrite is mechanically strong (fracture toughness higher than Yb:YAG and Ti:Sapphire [6,7]), has relatively high thermal conductivity (κ: ~28 W/K.m [8] compared to 10 W/K.m of Yb:YAG [7]), has an intrinsic slope efficiency of 65% [9,10], and can be grown with very low passive losses[9]. In the early years of its development, these favorable properties made Alexandrite the laser of choice in the development of flashlamp pumped high energy and high power Q-switched laser systems especially for biomedical applications. Over the last decade, the advancement of higher brightness laser and light-emitting diodes in the red spectral region, generated a renewed interest towards Alexandrite [11–25] and continuous-wave laser output powers above 25 W have already been achieved from compact diode-pumped systems [12]. Mode-locking of Alexandrite using Saturable Bragg Reflectors (SBRs) [26], Kerr-lensing [27,28], and graphene saturable absorbers [29] has also been demonstrated recently.

Unlike simple laser systems such as Yb:YAG, Alexandrite has a complex energy level diagram (Fig. 1 (a)), which creates quite interesting and unique laser properties that provide both pros and cons in terms of laser operation. In Alexandrite, the broadband lasing occurs via the phonon widened $^4T_2 \rightarrow {}^4A_2$ transition. Note, that the intrinsic lifetime of the higher lying $^4T_2$ laser level used in this broad emission is only around 6.6 µs, which, by itself, is too short for effective lasing or effective flashlamp pumping. However, the $^4T_2$ energy level is coupled to the lower lying

#368087 https://doi.org/10.1364/OME.9.003352
Journal © 2019 Received 20 May 2019; revised 28 Jun 2019; accepted 1 Jul 2019; published 12 Jul 2019

Optical Materials EXPRESS

metastable ^{2}E level, which has an intrinsic lifetime of around 1.54 ms [4]. In thermal equilibrium, excited ion densities in each level are determined by Boltzmann statistics. In Alexandrite, the energy difference between the $^4T_2$ and ^{2}E states (ΔE: 800 cm^{-1}) is only a few kT (200 cm^{-1}) at room temperature. As a result, significant portion of the excited ions are located in the $^4T_2$ state and could contribute to the broadband emission. This coupling process also increases the effective radiative lifetime (τ_R) of the $^4T_2$ level to around 260 μs at room temperature, enabling adequate storage upon pulsed pumping, and low-threshold and efficient laser operation. In comparison, in ruby, which possesses an almost identical energy band diagram, ΔE is around 2300 cm^{-1}, which is too high to obtain sufficient population densities in the $^4T_2$ state, preventing broadly tunable laser emission [30].

At temperatures above room temperature, the increased phonon energy (kT) accelerates the interaction between the $^4T_2$ and ^{2}E energy states of Alexandrite and raises the ratio of ions residing in the $^4T_2$ level. Hence, the effective emission cross section of the $^4T_2$ level (σ_{em}) increases at the expense of reduced effective radiative lifetime (τ_R). The normalized emission cross section curves of Alexandrite given at 25 °C and 400 °C in Fig. 1 (b) clearly show the result of this process on the emission spectra: with increasing temperature the narrowband emission from the $^2E \rightarrow {}^4A_2$ transition gets weaker, and the broadband emission from the $^4T_2 \rightarrow {}^4A_2$ gets stronger. Note that, emission spectra will only be given for the E//b axis throughout this paper, since it dominates the lasing properties in Alexandrite (emission strength is an order of magnitude weaker for the E//a and E//c axis).

Interestingly, as earlier studies have shown already, in Alexandrite, the gain product (the product of effective emission cross section and fluorescence lifetime: $\sigma_{em}\tau_F$) increases with temperature and has a maximum at a temperature of around 100 °C [3]. This is because, for some emission wavelengths, the rate of decrease in fluorescence lifetime is smaller than the rate of increase in effective emission cross section value, resulting in an increased gain product. We need to note here that, the process is actually more complex due to the presence of excited state absorption (ESA, σ_{esa}) and ground state absorption (σ_a) in the lasing wavelength region of Alexandrite. On top of these, excited state absorption also exists in the pumping wavelength region of Alexandrite [31]. The effect of pump excited state absorption on pumping efficiency has been discussed in [14,32,33]; and its temperature dependence is investigated in [33].

In a nutshell, the development of higher brightness red laser diodes over the last decade opened up the possibility to build efficient, low-cost and high power Alexandrite laser and

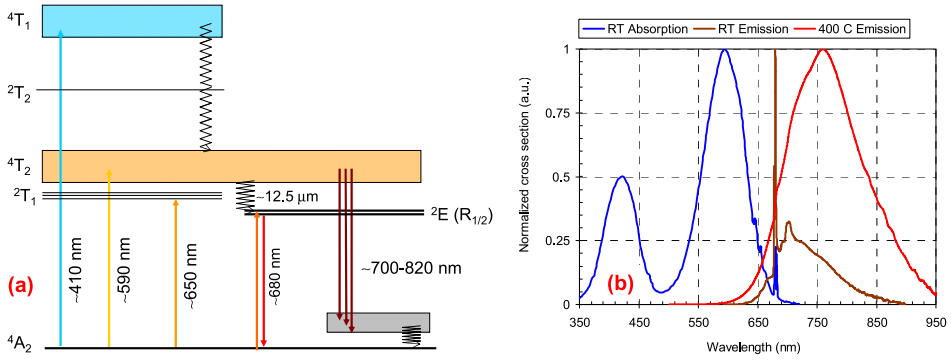


Fig. 1. (a) Simplified energy level diagram of Alexandrite laser gain medium. Broadband lasing occurs between the vibronically widened $^4T_2$ and $^4A_2$ levels. The metastable ^{2}E level acts as a reservoir (storage level), and similar to ruby, this level can also enable narrowband lasing around 680 nm (via $^2E \rightarrow {}^4A_2$ transition). (b) Normalized absorption and emission cross section of Alexandrite at room temperature (RT: 25 °C). Normalized emission spectrum of Alexandrite at 400 °C is also given. All spectra are given for E//b polarization.

Optical Materials EXPRESS

amplifier system. However, the progress has been relatively slow especially for the development of ultrashort pulse laser/amplifier sources, and there is currently a need for better understanding of Alexandrite laser gain media, for accurate modeling of its laser potential. Recent detailed work by Kerridge-Johns et al. on the effect of pump and laser excited state absorption on laser performance has been an important step towards this aim [14,32,33]; however, efforts in this direction face a challenge due to the limited availability of spectroscopic data. For a laser design engineer, a thorough modeling of laser dynamics and its potential as an efficient laser requires detailed knowledge of wavelength and temperature dependence of all the relevant cross sections (σ_{em}, σ_{esa}, and σ_a) as well as the temperature dependence of fluorescence lifetime (τ_F). The thermo-opto-mechanical properties of the gain media should also be known, which recently motivated Loiko et al. for the measurement of second and third order dispersive properties, and dn/dT parameters in Alexandrite [34,35].

As a more specific example, over the last years, several groups have been working on the development of ultrashort pulse Alexandrite laser systems [26–29], which resulted in the generation of down to 70-fs long pulses with average output powers in the multi-mW to multi-100 mW range. Unfortunately, mode-locking is only demonstrated in systems pumped by complex green laser sources so far. There is also very limited work studying the ultrafast amplification potential of Alexandrite gain media [36,37]. On the other hand, diode-pumped Alexandrite laser/amplifier systems have the potential to generate sub-20-fs long pulses with multi-10-W average power levels, which will be of great interest for many scientific and engineering applications. This potential creates a strong research interest towards Alexandrite gain media. As discussed briefly above, to accurately determine Alexandrite's ultrashort pulse generation/amplification capabilities, small signal optical gain of Alexandrite should be studied in detail as a function of temperature and wavelength. Unfortunately, there is quite limited information on temperature and wavelength dependence of effective emission cross section (σ_{em}) and excited state absorption (σ_{esa}) cross sections of Alexandrite in the existing literature [2,31,38], which currently limits accurate modeling of this important laser gain medium.

Motivated by the above observations, in this study we have first carefully measured the effect of temperature on the effective emission cross section (σ_{em}) spectra of Alexandrite in the 25-450 °C range. Then, from the measured effective emission cross section data, we have extracted analytical formulas that allow accurate prediction of temperature and wavelength dependence of σ_{em} data. Moreover, the results are combined with the excited state absorption data from the literature [38] to estimate the effective gain line shapes at different temperatures, and detailed comparison with earlier experimental data have been performed for confirmation of the models accuracy. Variation of the net small signal gain as a function of temperature is also investigated for several different wavelengths, which confirmed the measured improvement in laser performance with temperature [3,13,14,39]. To our knowledge, this is the first detailed study presenting the temperature dependence of the effective emission cross section and small signal gain spectra in Alexandrite. We hope that the data provided in this work will become a valuable resource for researchers working on Alexandrite laser systems.

The paper is organized as follows: Section 2 presents the effective emission cross section measurements in detail. Section 3 uses the measured effective emission cross section data and investigates wavelength and temperature dependence of laser gain, and provides comparison with experimental results in the literature. Finally, in section 4, we briefly summarize the results.

2. Emission cross section measurements

2.1. Experimental setup

Figure 2 shows a simplified schematic of the emission cross section measurement setup used in this study. A methodology similar to what was employed in [2,38,40,41] was used in the measurements. A linearly polarized 632.8 nm He-Ne laser with around 1 mW of output power

Optical Materials EXPRESS

excited the laser gain medium. A band-pass filter (BPF) around 630 nm was used just after the pump laser to cut all the other weak emission lines of He-Ne. The Alexandrite crystal was Brewster cut, 8-mm-long and had a chromium-doping level 0.13%. Using spectrometer 1 (Spec 1) and a film polarizer (P), the fluorescence spectrum is measured for the b and c axis. From the other side of the crystal the fluorescence spectra in the a and c axis are measured using a similar procedure. The repeated measurement of the fluorescence spectra in the c axis enabled standardization of the emission rates in these independent measurements. The temperature of the crystal was controlled by using two soldering iron heater heads in direct contact with the crystal, and the crystal temperature was measured at 3 independent points for confirmation of thermal equilibrium. The emission spectra were measured between 25 °C and 450 °C in discrete steps of 25 °C. The spectrometer used for the measurements was based on a 3648 pixel CCD array (Toshiba TCD1304AP) and it had had a spectral resolution of 0.2 nm in the 190-1100 nm range. The overall spectral response of the measurement system (CCD array, grating, film polarizer) was corrected using spectral response curves provided by the companies and our spectral response correction was then confirmed with measurements performed with broadband emission sources with known spectral distribution. We estimate an accuracy better than ±30% in our fluorescence intensity measurements in the 550-850 nm range, and an accuracy better than ±60% above 850 nm (we have larger error bars at longer wavelengths due to the reduced sensitivity of the CCD array).

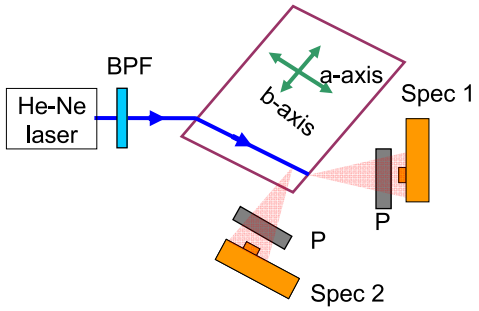


Fig. 2. A simplified schematic of the setup used for fluorescence measurements of Alexandrite crystals. The Alexandrite crystal was an a-cut sample, with the axes oriented as shown. BPF: band-pass-filter, P: film polarizer, Spec 1: Spectrometer used for measuring the emission spectrum in the b and c axis, Spec 2: Spectrometer used for measuring the emission spectrum in the a and c axis.

2.2. *Fluorescence intensity measurement results*

The measured temperature dependent fluorescence spectra of the Alexandrite gain medium in the 550-950 nm range for E//b polarization are shown in Fig. 3. As also discussed above, due to the coupling of the vibronically broadened $^4T_2$ level and the narrowband metastable ^2E level, the measured emission spectra of Alexandrite are structured and possess different emission peaks. In Fig. 3 (a), the spectra are normalized to the peak of emission cross section, whereas in Fig. 3 (b) the measured fluorescence spectra are normalized to the peak value of emission for the broadband $^4T_2 \rightarrow {}^4A_2$ transition. The shape of the measured fluorescence spectrum is in good agreement with the measurements done using calibrated spectral systems in the literature [2,38,42,43]. Note, however that, the fluorescence spectra of Alexandrite might show some differences depending on the excitation wavelength as discussed in [41,43–45]. In our study, a 632.8 nm He-Ne laser was chosen for excitation since it lies at the lower wavelength edge of the main emission spectrum, and could be easily distinguished and removed from the Alexandrite

Optical Materials EXPRESS

emission spectra (spectral peak of the pump source is electronically removed from the emission spectrum measurements shown in this work). Moreover, this wavelength is close to the emission peak of high brightness red laser diodes (630-680 nm), that can be used for efficient excitation of Alexandrite systems. As a side note, we on purpose did not use an excitation wavelength in the green or blue regions of the spectrum, since pumping at these wavelengths (i) cause larger quantum defect, and (ii) is believed to produce chaotic cw lasing in Alexandrite via the coupling of excess phonon population produced in pumping [44,46].

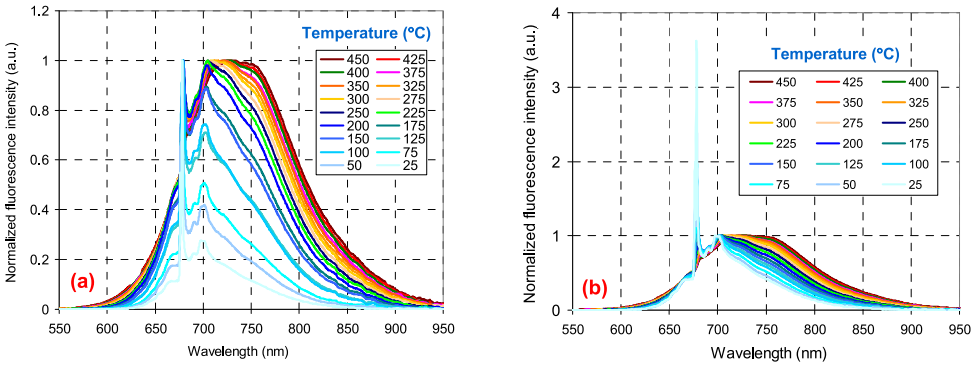


Fig. 3. Measured emission fluorescence spectra of Alexandrite for E//b polarization at crystal temperatures ranging from 25 °C to 450 °C. In (a) spectra are normalized to the peak emission wavelength intensity, whereas in (b) spectra are normalized to the peak of phonon broadened $^4T_2 \rightarrow {}^4A_2$ transition. The peak corresponding to the pump laser (He-Ne) emission at 632.8 nm is electronically removed from the measurements.

2.3. Normalized emission cross section curves

To initiate a more accurate discussion on spectral shape of the emission spectra, in Fig. 4 we plot the calculated normalized effective emission cross section spectrum ($\sigma_e(\lambda)$) of Alexandrite at different temperatures. The normalized emission cross section curves are obtained by multiplying the measured fluorescence emission spectrum by a factor of λ^5 (where λ is the emission wavelength) [40,47], and then renormalizing the curves to the peak value of $^4T_2 \rightarrow {}^4A_2$ transition. Note that, the emission spectrum has several underlying peaks around 680 nm, 700 nm, 720 nm and 750 nm. The emission peaks around 680 nm and 750 nm are well-known and attributed to the $^2E \rightarrow {}^4A_2$ and $^4T_2 \rightarrow {}^4A_2$ transitions, respectively. We could not find detailed spectrospic identification of the other emission peaks in the literature [43], but these peaks might be due to strong phonon-electron coupling effects (a similar phenomenon creates emission side peaks in Yb:YLF [48]). There are a few interesting points to emphasize here. First of all, as expected from Boltzmann occupation probability distribution, the effective emission cross section strength of the metastable ^2E level decreases with increasing temperature (the emission peak around 680 nm loses its strength). This is because more of the excited chromium ions occupy the phonon broadened $^4T_2$ state, leaving a smaller portion of the ions in the lower lying metastable ^2E state. Additionally, with increasing temperature, the peak of the emission spectrum moves to longer wavelengths (Fig. 5). Moreover, the width (FWHM: full-width-half-maximum) of the phonon broadened emission spectra increases with rising temperature values (Fig. 5).

In closing this sub-section, in Fig. 6, we provide the measured normalized emission cross section curves for Cr:LiCAF and Cr:LiSAF at room temperature (RT: 25 °C) together with the emission curves of Alexandrite at RT and at 300 °C. All of these gain media can be pumped by low-cost red laser diodes around 640 nm, and provide broadly tunable lasing in a spectral region similar to Ti:Sapphire [40,49–53]. The measured emission spectrum curves of Cr:LiSAF

Optical Materials EXPRESS

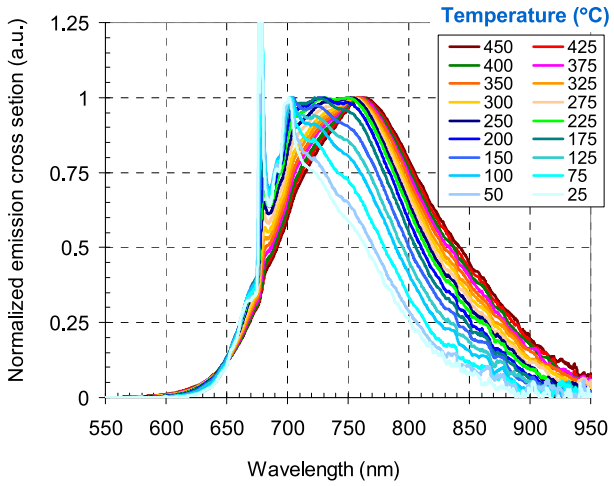


Fig. 4. Calculated emission cross section spectra of Alexandrite for E//b polarization at crystal temperatures ranging from 25 °C to 450 °C. The spectra are normalized to the peak of the phonon broadened $^4T_2 \rightarrow {}^4A_2$ transition.

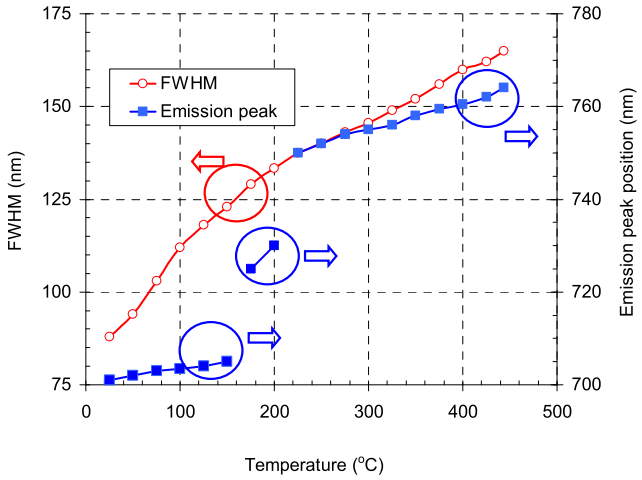


Fig. 5. Measured variation of Alexandrite emission peak and emission spectrum width (FWHM) as a function of temperature for the phonon broadened $^4T_2 \rightarrow {}^4A_2$ transition.

and Cr:LiCAF also match relatively well the emission spectra provided in literature [54,55], confirming the spectral calibration of the measurement system within the measurement error bars. Note that, a second InGaAs detector was used for the measurement of emission cross section of Cr:LiSAF above 950 nm (the curves are combined electronically around a wavelength of 960 nm).

2.4. *Radiative and fluorescence lifetime of Alexandrite*

So far, we have only provided normalized emission cross section curves for Alexandrite. In the next sub-section, we will calculate and provide absolute values for emission cross sections, but this requires knowledge of the dependence of radiative lifetime of upper laser level to temperature (τ_R(T): also known as spontaneous-emission lifetime [56]), which will be discussed in this sub-section. As mentioned earlier, due to the strong coupling between the metastable ^{2}E level

Optical Materials EXPRESS

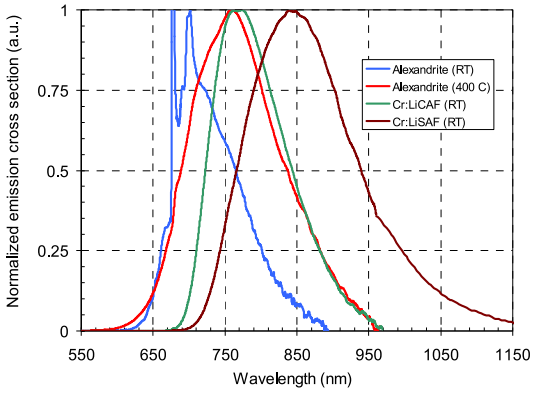


Fig. 6. Calculated normalized emission cross section curves for Alexandrite, Cr:LiCAF and Cr:LiSAF at room temperature (RT). For Alexandrite, the emission cross section curve at 400 °C is also shown.

with the phonon broadened $^4T_2$ level, we need to consider the lifetime of upper laser level of Alexandrite as an effective lifetime that varies with the strength of the interaction. The intrinsic radiative lifetime of the metastable ^2E storage level (τ_E) is 1.54 ms, whereas the intrinsic radiative lifetime of the phonon-broadened $^4T_2$ upper state laser level (τ_T) is only 6.6 µs. The strength of interaction between these levels as well as the effective radiative lifetime (τ_R) of the system is temperature dependent and could be calculated using [57,58]:

$$\frac{1}{\tau_R(T)} = \frac{1}{\tau_E} p_E(T) + \frac{1}{\tau_T} p_T(T), \tag{1}$$

where $p_E(T)$ and $p_T(T)$ are the temperature dependent radiative transition probability (relative population density) of the ^2E storage level and the $^4T_2$ upper state laser level, respectively. Assuming quasi-thermodynamic equilibrium, using Boltzmann statistics, one can derive the following formula for the estimation of effective radiation lifetime [57,58]:

$$\tau_R(T) = \tau_E \frac{1 + Exp\left(-\frac{\Delta E}{k(T+273)}\right)}{1 + \frac{\tau_E}{\tau_T} Exp\left(-\frac{\Delta E}{k(T+273)}\right)}, \tag{2}$$

where ΔE is the activation energy for phonon coupling between the storage and laser levels (800 cm^{-1}), k is the Boltzmann constant, and T is the temperature in units of °C (See Fig. 1 (a)).

Figure 7 shows the variation of effective radiative lifetime of the upper laser level (τ_R) with temperature calculated using Eq. (2). Note again that, this is the effective radiative lifetime of the Alexandrite crystal, and the decrease in lifetime is not due to the existence of non-radiative processes, but due to the interaction between the ^2E and $^4T_2$ levels. At low temperatures the population of ions in the $^4T_2$ energy level can be ignored ($p_T \sim 0$) and the radiative lifetime approaches the intrinsic radiative lifetime of the meta-stable ^2E level (1.54 ms). On the contrary, at high temperatures, most of the excited ions lie in the higher lying $^4T_2$ level ($p_T \sim 1$), and as the temperature tends to infinity, the effective radiative lifetime of the system approaches two times the intrinsic lifetime of the $^4T_2$ level (~13.2 µs).

The radiative quantum efficiency of a laser material (η_{RE}) is defined as the average number of fluorescent photons per an excited ion in the upper laser level [59], and determines the ratio of useful radiative/fluorescent transitions from the upper laser level. Interestingly, the radiative quantum efficiency of Alexandrite at low temperatures is measured to be close to unity (0.95

Optical Materials EXPRESS

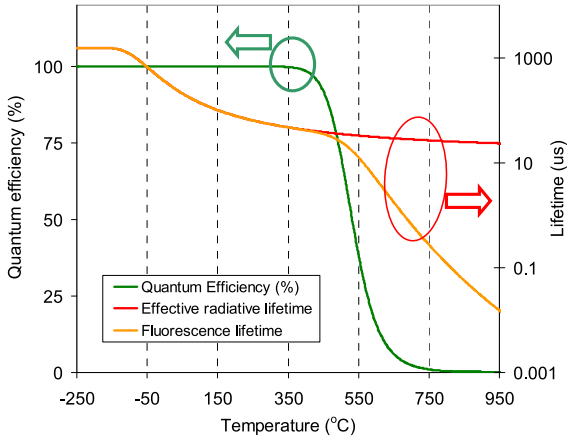


Fig. 7. Calculated variation of the radiative quantum efficiency, effective radiative lifetime and fluorescence lifetime for Alexandrite as a function of temperature.

±0.05) for temperatures up to 400 °C [57,58]. Hence, the fluorescence lifetime (τ_F), which is also known as the laser upper-state lifetime, is almost identical to radiative lifetime for temperatures below ~350 °C. At elevated temperatures above ~350 °C, the ions at the upper laser level starts to decay to the laser ground state also via nonradiative process (known also as thermal quenching or multi-phonon emission). The temperature dependence of the fluorescence lifetime (τ_F) can then be determined with [58]:

$$\tau_F(T) = \tau_R(T)\eta_{RE}(T) \tag{3}$$

$$\eta_{RE}(T) = \left(1 + \frac{\tau_E}{\tau_{NR0}} Exp\left(-\frac{\Delta E_{NR}}{k(T+273)}\right)\right)^{-1}, \tag{4}$$

where τ_R(t) is the effective radiative lifetime, η_{RE} is the radiative quantum efficiency (τ_F(T)/τ_R(T)), ΔE_{NR} is the activation energy for nonradiative process (~12000 cm^{-1}), τ_{NR0} is the high temperature limit of the nonradiative lifetime (~0.75 ps). Note that the formula given above provides a good fit to the measured radiative quantum efficiency data reported in [58]; but we have used a simpler functional form for simplicity (see Eq. 5 in [58]). The calculated variation of radiative quantum efficiency and fluorescence lifetime with temperature using Eqs. (3)–(4) are also shown in Fig. 7. We note here that, due to radiation trapping, the measured fluorescence lifetime values of Alexandrite in the literature show some variation depending on the chromium doping of the samples used. Especially, the low temperature (cryogenic) measurements show a larger variation from sample to sample due to the larger overlap between the absorption and emission bands at low temperatures [13,58]. On the other hand, at room temperature and above, which is our main interest in this work, radiation trapping effects diminish and lifetime data are more consistent. In this work, we have chosen to use τ_E (1.54 ms), τ_T (6.6 µs) and ΔE (800 cm^{-1}) values reported by Walling et al. [2], since they have used a very lightly chromium doped (<0.0005%) Alexandrite sample, which should minimize radiation trapping effects. The measured fluorescence lifetime of the Alexandrite sample used in this study [19] matches very well (±10 µs) to the numerical values calculated using Eqs. (3)–(4). Note also that, the critical temperature ($T_{1/2}$) at which the nonradiative transitions become as strong as radiative transitions is around 530 °C in Alexandrite. In comparison the critical temperature for thermal quenching ($T_{1/2}$) is only around 250 °C in Cr:LiCAF [60], 80 °C in Ti:Sapphire [40,61], 70 °C in Cr:LiSAF [60]. Combined with its known mechanical strength, this unique thermal property gives Alexandrite a great advantage in power scaling compared to the aforementioned gain media [12,62].

Optical Materials EXPRESS

2.5. Emission cross section curves in absolute units

In this subsection, we will provide the emission spectrum curves for Alexandrite in absolute units. The emission cross section for Alexandrite gain media in E//b axis can be calculated using the modified Füchtbauer–Ladenburg formula [40,41,56]:

$$\sigma_{em}(\lambda) = \frac{\lambda^5}{8\pi c n^2 \tau_R} \frac{I_b(\lambda)}{\int \left(\frac{1}{3}I_a(\lambda) + \frac{1}{3}I_b(\lambda) + \frac{1}{3}I_c(\lambda)\right) \lambda d\lambda}, \tag{5}$$

where $I_{a,b,c}(\lambda)$ are the measured emission intensities in the a, b, c axis of the biaxial crystal, c is the speed of light, n is the refractive index of the gain medium, and other parameters are same as defined above. Figure 8 shows calculated effective emission cross section curves of Alexandrite at different temperatures (detailed explanation of effective emission cross section concept can be found in [2,56,63]). Within experimental erroŕ (±30%), the data is similar to what has been published in the literature earlier [2,38]. For example, the effective emission cross section value at 750 nm has been reported as 0.7×10^{-20} cm^2, 2.2×10^{-20} cm^2 and 3.9 x 10^{-20} cm^2 at temperatures of 28 °C, 150 °C and 300 °C in [38]. In comparison, we have found values of 0.65×10^{-20} cm^2, 2.17×10^{-20} cm^2 and 4.48 x 10^{-20} cm^2 for the same set of points, indicating good agreement with the literature results. As another example, the effective emission cross section value at 800 nm has been reported as 0.35×10^{-20} cm^2, 1.4×10^{-20} cm^2 and 3×10^{-20} cm^2 in [38] at temperatures of 28 °C, 150 °C and 300 °C, whereas we have measured values of 0.28×10^{-20} cm^2, 1.17×10^{-20} cm^2 and 3.07 x 10^{-20} cm^2 at the same temperatures.

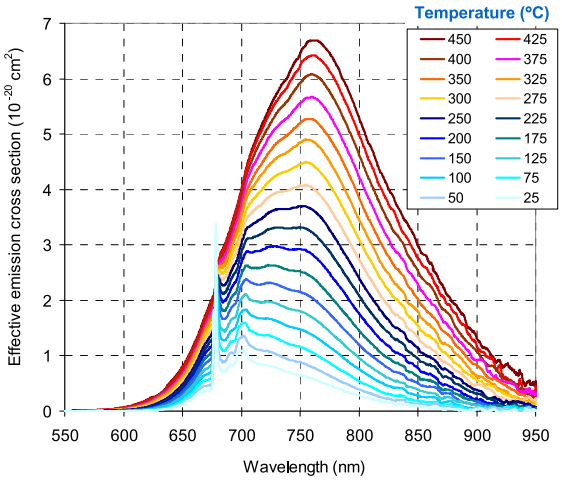


Fig. 8. Calculated effective emission cross section spectra of Alexandrite for E//b polarization at crystal temperatures ranging from 25 °C to 450 °C.

To know the dependence of the effective emission cross section on wavelength and temperature is important for the optimization of laser and amplifier performance. In that sense, here we present a set of functions that can be easily used in estimating $\sigma_{em}(\lambda,T)$ in numerical simulations. For that purpose, we have first tried to use a Lorentzian function to fit the curves in Fig. 8, but the fits deviated too much from the measured spectra. Instead, similar to what has been performed for Ti:Sapphire in [47], a Poisson distribution curve defined by four parameters (a, m, ν_0 and ν_p) has been used as the functional form:

$$\sigma_{em}(\lambda, T) = a\frac{m^P}{\Gamma(1+P)}, \tag{6}$$

Optical Materials EXPRESS

where P is defined as $(\nu_0\text{-}\nu)/\nu_p$, ν is the wave number $(1/\lambda)$, a is the normalization factor that maps the spectral-line shape to absolute emission cross section values. Above Γ is the Gamma (factorial) function that is calculated via the following Euler Integral:

$$\Gamma(1+P) = \int_0^\infty x^P e^{-x} dx. \tag{7}$$

Note, that in Eq. (6), a, m and P (ν_0 and ν_p) are temperature dependent fit parameters. The least squares fit parameters to the experimental data for different crystal temperatures are listed in Table 1. Figure 9 shows the experimentally measured emission cross section curves along with the numerical curves obtained using Eq. (6) with the best fit parameters listed in Table 1. Note that, especially for low temperatures, the emission spectra are quite structured hence the numerical fit is useful in a limited spectral range. For that purpose, Table 1 also includes information on the spectral range where the fit between the experimental data and the Poisson distribution is relatively good. Note that the valid range of the fits fully covers the tuning range of Alexandrite as a gain medium.

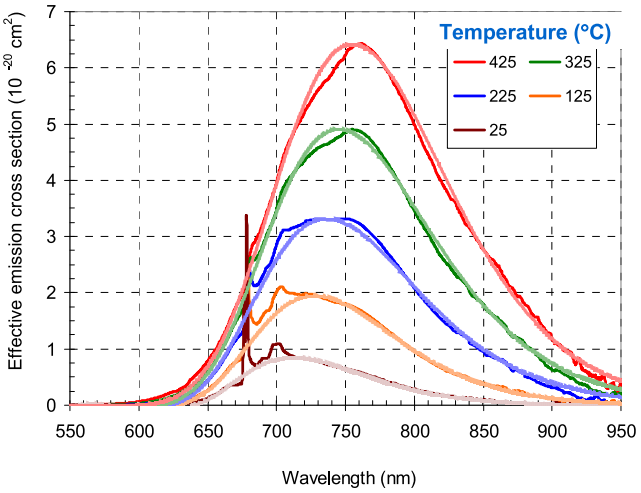


Fig. 9. Poisson distribution fit to selected effective emission cross section curves. The darker solid lines are experimental data, whereas the light solid lines are the fitted curves.

Equation (6) provides information on the dependence of effective emission cross section on wavelength at selected temperatures. A knowledge of variation of effective emission cross section with temperature at a fixed wavelength is also useful in the design of laser/amplifier systems. For that purpose, Fig. 10 shows the measured dependence of the effective emission cross section on temperature for selected wavelengths in the range from 675 nm to 950 nm. Variation of the peak value of the emission cross section with temperature is also shown in Fig. 10. Note that, in Fig. 7 of [2], similar trend curves are provided in the temperature range from 25 °C to 200 °C; however, only for wavelengths of 750 and 780 nm. We note that, our values reported in Fig. 10 are slightly higher than what is reported in Fig. 7 of [2], but fit relatively well to the values reported in [38] by same group of authors. Note that, the trend for each wavelength is different. For some wavelengths the slope decreases and saturates (especially for short wavelengths such as 675 and 700 nm). On the other hand, for long wavelengths (such as 925 and 950 nm) initially the emission cross section values are quite small and an increasing trend is observed only at higher temperatures.

Optical Materials EXPRESS

Table 1. Poisson distribution fit results for Eq. (6).*

Temperature (°C)	Spectral range (nm)	m	ν_0 (cm^{-1})	ν_p (cm^{-1})	1/a
25	715-900	2.3	15061	575	(1.58)2!
50	715-900	2.7	15161	546	(1.65)2!
75	715-900	3.9	15432	460	(1.22)3!
100	710-900	4.7	15626	433	(2.02)3!
125	710-900	5.4	15780	417	(3.28)3!
150	710-900	6.2	15935	395	(1.43)4!
175	710-900	9	16453	333	(3.42)5!
200	650-870*	5.3	15817	450	(1.96)3!
225	650-870*	5.7	15881	443	(2.53)3!
250	650-870*	7.2	16209	396	(2.26)4!
275	650-880*	8.4	16436	369	(1.26)5!
300	650-880*	10.4	16744	333	(1.26)6!
325	650-900*	12	16992	310	(5.32)6!
350	650-900	14.1	17284	288	(5.32)7!
375	650-900	15.7	17497	274	(2.91)8!
400	650-900	20.3	18051	241	(2.63)10!
425	650-900	25.1	18609	218	(2.06)12!
445	650-900	33.7	19478	189	(3.40)15!

* Fit results provide a good match in the specified spectral range except for the 680 nm transition.

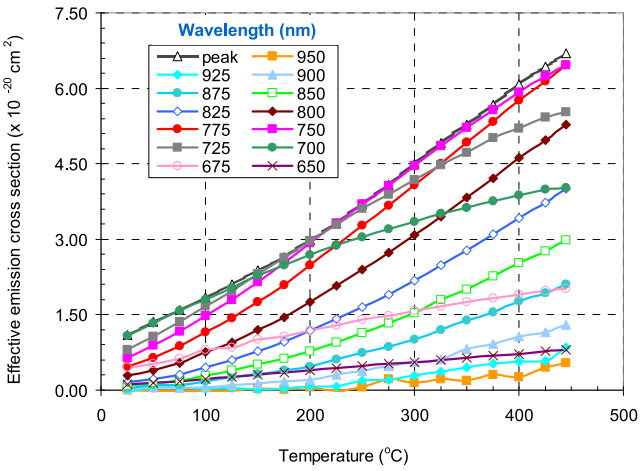


Fig. 10. Estimated variation of the effective emission cross section of Alexandrite with temperature at selected wavelengths for the E//b polarization.

As a specific example, in our calculations, we have shown that the emission cross section value at 750 nm increases from 0.65×10^{-20} cm^2 to 5.93×10^{-20} cm^2 when the temperature increases from 25 °C to 400 °C (a 9 fold increase in effective emission cross section value). As another example, the effective emission cross section value at 700 nm increases from 1.09×10^{-20} cm^2 to 3.87×10^{-20} cm^2 when the temperature increases from 25 °C to 400 °C (only a 3.55 fold increase). From Fig. 7, we see that the radiative lifetime decreases from 260 µs to 35.6 µs upon the rise of temperature from 25 °C to 400 °C (a 7.3 fold decrease in radiative lifetime). From

Optical Materials EXPRESS

Eq. (5), we know that, for a fixed shape of the emission spectrum, a 7.3 fold decrease in the radiative lifetime should create a 7.3 fold increase in the effective emission cross section. On the other hand, the spectral shape of the emission curve varies considerably with temperature (the 680 emission band disappears and the phonon broadened emission widens and its centre shifts to longer wavelengths); hence, depending on the wavelength, the increase in the emission cross section can be larger or smaller than 7.3. As will be discussed in the later sections, this results in different optimum crystal temperatures for lasing at different wavelengths.

We close this section with Table 2, which provides equations for estimating the effective emission cross section as a function of temperature at selected wavelengths (least squares fit to the data presented in Fig. 10). Note that a relatively complex functional form of:

$$\sigma_{em}(\lambda,T) = a_o + a_1T + a_2T^2 + a_3T^3 + a_4T^4 \quad (8)$$

has been chosen in order to obtain a fitting curve that could provide physically relevant emission cross sections (e.g. values ≥0) in a wider range of temperatures (0 °C to 500 °C). Note, again the coefficients a_0 - a_4 in Eq. (8) are wavelength dependent fit parameters.

Table 2. Best fit values of the temperature coefficients in Eq. (8) for the calculation of effective emission cross section at different temperatures.

Wavelength (nm)	a_o	a_1 ($°C^{-1}$)	a_2 ($°C^{-2}$)	a_3 ($°C^{-3}$)	a_4 ($°C^{-4}$)
650	9.81×10^{-2}	1.03×10^{-3}	2.40×10^{-6}	-1.23×10^{-9}	-3.27×10^{-12}
675	3.81×10^{-1}	3.31×10^{-3}	5.14×10^{-6}	-8.32×10^{-9}	-3.42×10^{-12}
700	9.54×10^{-1}	7.87×10^{-3}	8.23×10^{-6}	-2.79×10^{-8}	9.45×10^{-12}
725	6.98×10^{-1}	7.76×10^{-3}	2.03×10^{-5}	-9.44×10^{-9}	-4.73×10^{-11}
750	5.23×10^{-1}	7.06×10^{-3}	2.52×10^{-5}	4.36×10^{-9}	-6.67×10^{-11}
765	4.15×10^{-1}	6.28×10^{-3}	2.58×10^{-5}	1.16×10^{-8}	-6.90×10^{-11}
775	3.40×10^{-1}	5.56×10^{-3}	2.46×10^{-5}	1.45×10^{-8}	-6.51×10^{-11}
800	1.81×10^{-1}	3.61×10^{-3}	1.93×10^{-5}	1.82×10^{-8}	-4.94×10^{-11}
825	8.56×10^{-2}	2.21×10^{-3}	1.40×10^{-5}	1.70×10^{-8}	-3.41×10^{-11}
850	3.96×10^{-2}	1.35×10^{-3}	9.95×10^{-6}	1.46×10^{-8}	-2.31×10^{-11}
875	1.79×10^{-2}	7.85×10^{-4}	6.43×10^{-6}	1.09×10^{-8}	-1.24×10^{-11}
900	1.89×10^{-3}	2.80×10^{-4}	3.28×10^{-6}	7.68×10^{-9}	-3.65×10^{-12}
925	4.84×10^{-4}	4.11×10^{-5}	1.15×10^{-6}	4.74×10^{-9}	3.21×10^{-12}
950	0	-5.66×10^{-5}	4.08×10^{-7}	3.24×10^{-9}	4.38×10^{-12}
peak	9.89×10^{-1}	6.32×10^{-3}	1.77×10^{-5}	1.49×10^{-8}	-4.87×10^{-11}

3. Predictions based on measured emission cross section spectra

In this section, we use our temperature and wavelength dependent emission cross section measurements to calculate the gain spectra of Alexandrite at different temperatures. However, besides the emission cross section curves, ground-state absorption cross section spectra (for estimation of self-absorption losses), and excited state absorption cross section spectra at the lasing wavelength region should also be considered. The ground-state absorption cross section at the lasing wavelength region can be estimated accurately using the extended McCumber theory [64]:

$$\sigma_a(E,T) = \sigma_e(E,T)Exp\left(-\frac{E-E*}{kT}\right), \quad (9)$$

where E is the energy of the photons, σ_e(E,T) is the effective emission cross section at energy E and temperature T, and E* is the effective zero phonon energy level. Note that E* is also

Optical Materials EXPRESS

temperature dependent [2,64] and has a value of 14701 cm^{-1} at room temperature (corresponds to a wavelength of 680.23 nm). On the other side, the excited state absorption spectra of Alexandrite is available in the literature for the temperature range from 28 °C to 290 °C [38]. Unfortunately, especially the high temperature data in [38] have large error bars (±30% for data in the 28-85 °C range, and ±60% for data in the 150-290 °C range). However, to our knowledge this is the only data available in the literature and will be used with some precaution in the following analysis.

Figure 11 shows the measured effective emission cross section (ECS) spectra, calculated ground-state absorption (GSA) spectra and the excited-state absorption (ESA) spectra [38] all together, at the selected temperatures of 25 °C, 85 °C, 150 °C and 250 °C (since ESA curves are only available at these temperatures in [38]). The effective gain cross section (GCS) spectra ($\sigma_g(\lambda)$) are also shown in Fig. 11, which are calculated using:

$$\sigma_g(\lambda, T) = \beta[\sigma_e(\lambda, T) - \sigma_{esa}(\lambda, T)] - (1 - \beta)\sigma_a(\lambda, T), \tag{10}$$

where β is the fractional population inversion level (taken as 0.05 (5%) in our analysis), and all the other parameters are as defined above. Note that the small signal gain coefficient (g_0) could simply be calculated from $\sigma_g(\lambda,T)$ using:

$$g_o(\lambda, T) = \sigma_g(\lambda, T)N_{cr}, \tag{11}$$

where N_{cr} is the number density of the active Cr^{3+} ions in the Alexandrite sample. It is well known that, for Alexandrite, only around 78% of the doped Cr^{3+} ions are on sites with mirror symmetry, and these ions dominate the lasing properties (the rest of the ions are in the inversion sites: see Fig. 1 in [43]). As an example, for the 8 mm long (ℓ=0.8 cm), 0.13% Cr-doped sample used in this study, an effective gain cross section (σ_g) of 2×10^{-22} cm^2 corresponds to a small signal gain coefficient (g_0) of around 0.0071 cm^{-1} and a single pass fractional gain ($g_o\ell$) of around 0.0057, that would create a gain of 1.14% in a roundtrip for a standing wave cavity (N_{cr} is taken as $0.13 \times 0.78 \times 3.51 \times 10^{20}$ ions/cm^3 [65]).

Note also from Fig. 11 that, 3 different gain cross section spectra have been calculated for each temperature: one using the excited state absorption (ESA) cross section given in [38], and a second (and third) curve assuming an ESA value 30% lower (30% higher) than what is reported in [38]. Our aim is to show the effect of measurement errors on the calculated gain spectra, as [38] actually specifies error bars of ±30% for the 28 °C and 85 °C measurements and ±60% for the 150 °C and 250 °C measurements. Hence, the calculations in Fig. 11 should be considered as best effort estimates based on the availability of data. Detailed measurement of ESA cross sections for Alexandrite at elevated temperatures is required in future studies for a more accurate prediction of Alexandrite laser behavior especially for temperatures above 100 °C.

Looking at Fig. 11 (a)–(d) in detail, we see that, the effective gain cross section of Alexandrite increases with increasing temperature as expected (as a reminder this is under the assumption of a fixed inversion level of 5%). In particular, if we investigate the gain spectra calculated at 25 °C, we see that the gain peak is located at 750± 5 nm, and the FWHM of the gain spectra is around 70 nm. Reported free running laser wavelengths at room temperature agree with this simulation (e.g. 755 nm in [11]).We see that at short wavelengths, gain spectra are limited mainly by the self-absorption losses. The effect of excited state absorption on gain spectra on short wavelength tuning limit is minor: by itself ESA limits tuning below 690 nm, whereas self-absorption already lowers the gain below zero at a wavelength of 716± 2 nm for an inversion level of 5%. Note also that the inversion level will determine the short wavelength cut-off for positive gain (Fig. 12), and for strongly pumped systems, the tuning limit will be pushed to shorter wavelengths. As an example, for an inversion level of 20%, the short wavelength cut-off is around 702± 2 nm. A short wavelength tuning limit of 724 nm is reported in [11] at room temperature, and a short wavelength tuning limit of 714 nm is reported in [14] at a crystal holder base temperature of 10

Optical Materials EXPRESS

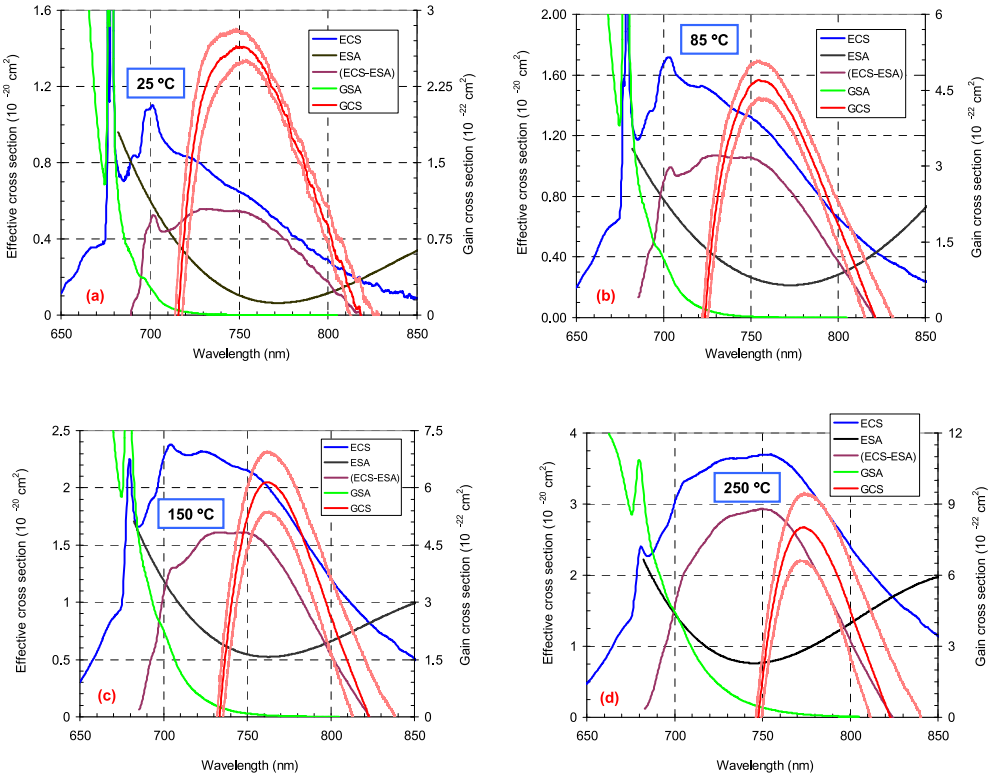


Fig. 11. Calculated gain cross section (GCS) at crystal temperatures of 25 °C, 85 °C, 150 °C and 250 °C. ESA: Excited state absorption, GSA: Grounds state absorption. Upper and lower values for gain cross section is also shown assuming ±30% error in ESA measurements. The calculations have been performed assuming a fixed inversion (β) level of 5%.

°C. Tuning down to 701 nm was obtained in [1] while pumping with high energy Xe-flashlamps. All of these results agree quite well with the estimates from the spectroscopic data. On the long wavelength side, excited state absorption at the lasing wavelength limits gain spectra and gain ceases at a wavelength of around 818 ± 5 nm at room temperature. A long wavelength tuning limit of 816 nm [11] and 818 nm [2,14] has been reported, which again matches the calculated room temperature gain spectra quite well.

At the temperature of 85 °C, the calculated gain spectra provide positive gain from 724 ± 2 nm to 821± 8 nm. First of all, compared to 25 °C for the fixed inversion level of 5%, the calculated gain cross section values are about 2-fold higher. Moreover, the short wavelength edge is shifted to longer wavelengths due to the shift of the absorption band towards longer wavelengths. The emission cross section curve itself also shifts to the long wavelength side, resulting in a gain peak position of around 758± 5 nm. The long wavelength cut-off is again limited by the onset of excited state absorption, and only shifts from around 816 nm to 821 nm with the increase of temperature from 28 °C to 85 °C. These observations are in good agreement with the experimental results in literature. For example, a cw tuning range extending from around 722 nm to 815 nm is reported in [14] at a crystal holder temperature of 60 °C.

At the temperature of 150 °C and 250 °C, a similar trend is observed in the gain spectra. Figure 13 (a) shows the calculated gain spectra at all the temperatures together for a better direct comparison. The gain peak shifts from around 750 nm to 775 nm as the temperature rises from 25 °C to 250 °C. The short wavelength cut-off edge shifts considerably to longer wavelengths

Optical Materials EXPRESS

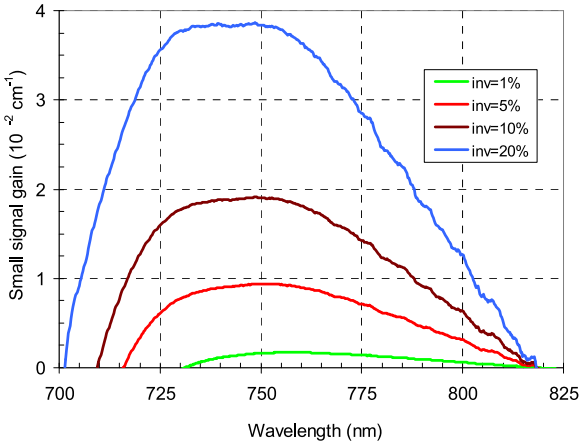


Fig. 12. Calculated variation of the small signal gain at a crystal temperature of 25 °C for inversion (β) levels of %1, %5, 10% and 20%.

mostly due to the increase in self-absorption losses (shift of the emission cross section peak to longer wavelengths only plays a very minor role in this shift). The long wavelength cut-off moves only slightly (1-2 nm) towards longer wavelengths owing to the strong and persistent excited state absorption band, limiting gain/amplification to below 820 nm in this temperature range. The detailed temperature dependent tuning results of [3] and [19] confirm this limitation in the investigated temperature range in this study (25-250 °C). As a result of the spectral changes, the FWHM of the gain spectra decreases from around 70 nm at 25 °C to around 60 nm at 85 °C, to 55 nm at 150 °C, and to 50 nm at 250 °C. Narrowing of the emission band will reduce the obtainable pulsewidths from the Alexandrite laser systems in mode-locked regime at elevated temperatures: the 25 °C gain spectrum enables sub-20-fs pulse generation/amplification whereas the attainable pulsewidths increases to around 30 fs at a temperature of 250 °C.

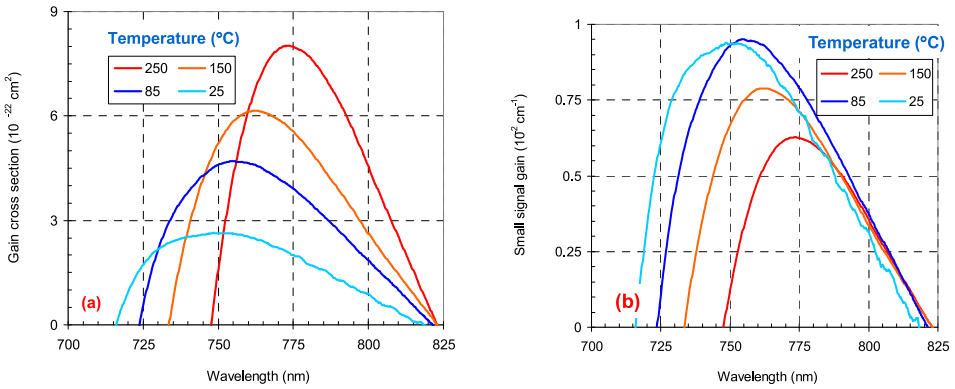


Fig. 13. (a) Calculated gain cross section (GCS) spectra at crystal temperatures of 25 °C, 85 °C, 150 °C and 250 °C. The calculation has been performed assuming a fixed inversion level of 5%. (b) Calculated small signal gain spectra at crystal temperatures of 25 °C, 85 °C, 150 °C and 250 °C. The calculation has been performed under fixed pumping rate assumption (due to the decreased fluorescence lifetime with temperature, inversion levels decrease at higher temperatures).

Optical Materials EXPRESS

In closing the discussion on ESA limitations on gain bandwidth, in [3] we see that at a temperature of 513 °C, the long wavelength tuning edge could be shifted up to 858 nm, which indicates that the emission cross section could overcome the limitations imposed by ESA at higher temperatures. Unfortunately, as mentioned earlier, detailed literature data about excited state absorption measurements at these temperatures are lacking, which limits our understanding of Alexandrite lasing behavior at elevated temperatures.

As we have mentioned earlier, in the gain cross section calculations, that we have made above, we had assumed a fixed inversion level of 5%. Under this assumption, as the temperature increases, due to the increase in the effective emission cross section, the gain cross section also increases. As an example, we see from Fig. 13 (a) that the peak gain cross section increases from around 2.65×10^{-22} cm^2 to 8×10^{-22} cm^2 as the temperature is increased from 25 °C to 250 °C. On the other hand, a fixed inversion level assumption is not always correct. As we have already mentioned above, as the temperature is increased from 25 °C to 250 °C, the radiative and fluoresce lifetime of Alexandrite decreases from 260 µs to 35.6 µs. Hence, for the fixed inversion assumption to be valid in the 25 °C to 250 °C temperature range, Alexandrite laser system should be pulse-pumped with pump pulses shorter than ~30 µs. In that respect, earlier pulsed pumping studies of Alexandrite agrees relatively well with the data in Fig. 13 (a). For example we see a significant reduction of lasing threshold pump energy with increasing temperature in [2], as well as a shift of gain spectra towards longer wavelengths that are both in good agreement with our analysis here (see Fig. 17 in [2]).

Under continuous-wave pumping at a fixed pump power fluence (or pumping rate), the inversion levels will actually decrease with temperature. To be more specific, for a fixed pumping intensity (I_p), under non-lasing conditions, ignoring the effect of pump excited state absorption, the fractional population inversion (β) could be estimated using [66] :

$$\beta(T) = \frac{I_p/I_{sa}}{1 + I_p/I_{sa}} \approx I_p/I_{sa}, \tag{12}$$

where I_{sa} is the pump absorption saturation intensity:

$$I_{sa} = \frac{hc}{\lambda_p \sigma_a \tau_f}. \tag{13}$$

Taking β at 25 °C as 0.05 (5%) as in our earlier calculations, the fractional inversion at other temperatures can be estimated using Eqs. (12)–(13). Note that a 5% inversion at room temperature corresponds to a pump intensity of around 0.05 I_{sat} (which translates into an intensity of ~0.5 kW/cm^2 for a pump wavelength of ~680 nm, and to a pump power of around 4.5 W for a 1 mm diameter pump beam).

The small signal gain coefficients calculated under a fixed pumping rate assumption are then shown in Fig. 13 (b). We see that, as expected, for each wavelength the small signal gain is optimized at a different crystal temperature. As an example, at the wavelength of 760 nm (gain peak of Alexandrite), the small signal gain at 85 °C is higher that the gain at 25 °C, 150 °C and 250 °C. To elaborate on this issue more, Fig. 14 shows the estimated small signal gain at selected wavelengths as a function of temperature. As a reminder the curve in Fig. 14 has error bars of around ±50%, at temperatures between 150-250 °C, due to the large error bars in the ESA measurements [38]. Moreover, we have used trend lines obtained from the 25-250 °C ESA data presented in [38], for estimation of ESA values above 250 °C; since, to our knowledge no data exist for laser ESA above 250 °C. Hence, the following analysis should be taken with some precaution, and future work is required for verification. It is clearly seen from Fig. 13 (b) and Fig. (Fig.14) that, for laser operation at shorter wavelengths (such as 725 nm), lower temperatures are better, since the increasing temperatures shift the small signal wavelength cutoff to longer wavelengths, limiting laser performance at elevated temperatures. On the other side of the gain

Optical Materials EXPRESS

peak, for wavelengths such as 750 nm and 775 nm, the optimum temperature lies around 100 °C. For even longer laser wavelengths, the optimum temperature is yet higher: around 300 °C for 800 nm, and above 400 °C for 825 nm. Despite the precautions we have mentioned above, we see that temperature dependent tuning results performed in literature (Fig. 17 in [2], Fig. 12 in [19], and Figs. 5–6 in [14]) agree quite well with these observations.

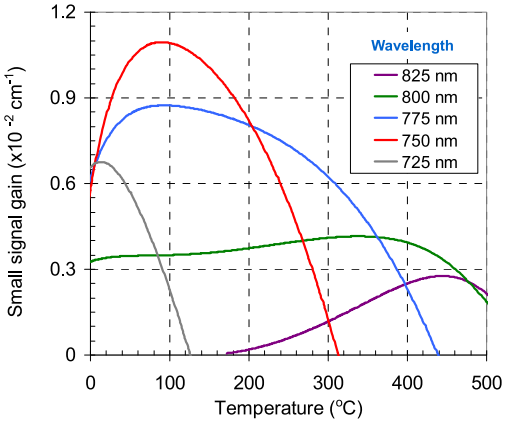


Fig. 14. Calculated variation of small signal gain with temperature at selected lasing wavelengths at a fixed pump intensity.

4. Conclusions

In conclusion, we have presented a detailed analysis of effective emission cross section spectra of the Alexandrite gain medium in the 25-450 °C temperature range. We have further provided analytical formulas that can be used to model the temperature and wavelength dependence of the effective emission cross section. We believe that these results will be useful in the accurate numerical simulation of next generation Alexandrite lasers and amplifiers. As an initial step, we have shown that the laser performance estimations based on the measured spectroscopic data provide a good fit to the observed experimental results documented in the literature. We also note that detailed measurements on the temperature dependence of excited-state absorption cross section spectra are required for better understanding of the Alexandrite laser medium.

Funding

Türkiye Bilimsel ve Teknolojik Araştirma Kurumu (TÜBITAK) (113F199); H2020 Marie Skłodowska-Curie Actions (MSCA) (PCIG11-GA-2012-321787); Alexander von Humboldt-Stiftung; Bilim Akademisi.

Acknowledgements

UD acknowledge support from the BAGEP Award of the Bilim Akademisi.

References

1. J. C. Walling, H. P. Jenssen, R. C. Morris, E. W. O'Dell, and O. G. Peterson, "Tunable laser performance in $BeAl_2O_4Cr^{3+}$," Opt. Lett. **4**(6), 182–183 (1979).
2. J. C. Walling, O. G. Peterson, H. P. Jenssen, R. C. Morris, and E. W. Odell, "Tunable Alexandrite Lasers," IEEE J. Quantum Electron. **16**(12), 1302–1315 (1980).
3. J. W. Kuper, T. Chin, and H. E. Aschoff, "Extended tuning of Alexandrite laser at elevated temperetures," in *Advanced Solid State Lasers* (OSA, Salt Lake City, Utah, 1990).

Optical Materials EXPRESS

4. J. C. Walling, D. F. Heller, H. Samelson, D. J. Harter, J. A. Pete, and R. C. Morris, "Tunable Alexandrite Lasers - Development and Performance," IEEE J. Quantum Electron. **21**(10), 1568–1581 (1985).
5. B. K. Sevast'yanov, "Excited-state absorption spectroscopy of crystals doped with Cr^{3+}, Ti3+, and Nd^{3+} ions. Review," Crystallogr. Rep. **48**(6), 989–1011 (2003).
6. B. W. Woods, S. A. Payne, J. E. Marion, R. S. Hughes, and L. E. Davis, "Thermomechanical and thermooptic properties of the $LiCaAlF_6$-Cr^{3+} laser material," J. Opt. Soc. Am. B **8**(5), 970–977 (1991).
7. L. J. Atherton, S. A. Payne, and C. D. Brandle, "Oxide and fluoride laser crystals," Annu. Rev. Mater. Sci. **23**(1), 453–502 (1993).
8. D. A. Vinnik, P. A. Popov, S. A. Archugov, and G. G. Mikhailov, "Heat conductivity of chromium-doped alexandrite single crystals," Dokl. Phys. **54**(10), 449–450 (2009).
9. R. Scheps, J. F. Myers, T. R. Glesne, and H. B. Serreze, "Monochromatic End-Pumped Operation of an Alexandrite Laser," Opt. Commun. **97**(5-6), 363–366 (1993).
10. S. A. Payne, L. L. Chase, H. W. Newkirk, L. K. Smith, and W. F. Krupke, "$LiCaAlF_6$:Cr^{3+} a promising new solid-state laser material," IEEE J. Quantum Electron. **24**(11), 2243–2252 (1988).
11. E. Beyatli, I. Baali, B. Sumpf, G. Erbert, A. Leitenstorfer, A. Sennaroglu, and U. Demirbas, "Tapered diode-pumped continuous-wave alexandrite laser," J. Opt. Soc. Am. B **30**(12), 3184–3192 (2013).
12. A. Teppitaksak, A. Minassian, G. M. Thomas, and M. J. Damzen, "High efficiency > 26 W diode end-pumped Alexandrite laser," Opt. Express **22**(13), 16386–16392 (2014).
13. M. Fibrich, J. Sulc, D. Vyhlidal, H. Jelinkova, and M. Cech, "Alexandrite spectroscopic and laser characteristic investigation within a 78-400 K temperature range," Laser Phys. **27**(11), 115801 (2017).
14. W. R. Kerridge-Johns and M. J. Damzen, "Temperature effects on tunable cw Alexandrite lasers under diode end-pumping," Opt. Express **26**(6), 7771–7785 (2018).
15. A. Munk, B. Jungbluth, M. Strotkamp, H. D. Hoffmann, R. Poprawe, J. Hoffner, and F. J. Lubken, "Diode-pumped alexandrite ring laser in single-longitudinal mode operation for atmospheric lidar measurements," Opt. Express **26**(12), 14928–14935 (2018).
16. U. Parali, X. Sheng, A. Minassian, G. Tawy, J. Sathian, G. M. Thomas, and M. J. Damzen, "Diode-pumped Alexandrite laser with passive SESAM Q-switching and wavelength tunability," Opt. Commun. **410**, 970–976 (2018).
17. S. Ghanbari and A. Major, "High power continuous-wave dual-wavelength alexandrite laser," Laser Phys. Lett. **14**(10), 105001 (2017).
18. M. J. Damzen, G. M. Thomas, and A. Minassian, "Diode-side-pumped Alexandrite slab lasers," Opt. Express **25**(10), 11622–11636 (2017).
19. I. Yorulmaz, E. Beyatli, A. Kurt, A. Sennaroglu, and U. Demirbas, "Efficient and low-threshold Alexandrite laser pumped by a single-mode diode," Opt. Mater. Express **4**(4), 776–789 (2014).
20. X. Sheng, G. Tawy, J. Sathian, A. Minassian, and M. J. Damzen, "Unidirectional single-frequency operation of a continuous-wave Alexandrite ring laser with wavelength tunability," Opt. Express **26**(24), 31129–31136 (2018).
21. G. M. Thomas, A. Minassian, X. Sheng, and M. J. Damzen, "Diode-pumped Alexandrite lasers in Q-switched and cavity-dumped Q-switched operation," Opt. Express **24**(24), 27212–27224 (2016).
22. E. A. Arbabzadah and M. J. Damzen, "Fibre-coupled red diode-pumped Alexandrite TEM00 laser with single and double-pass end-pumping," Laser Phys. Lett. **13**(6), 065002 (2016).
23. P. Pichon, A. Barbet, J. P. Blanchot, F. Druon, F. Balembois, and P. Georges, "LED-pumped alexandrite laser oscillator and amplifier," Opt. Lett. **42**(20), 4191–4194 (2017).
24. M. Fibrich, J. Šulc, and H. Jelínková, "Alexandrite microchip lasers," Opt. Express **27**(12), 16975–16982 (2019).
25. G. Tawy and M. J. Damzen, "Tunable, dual wavelength and self-Q-switched Alexandrite laser using crystal birefringence control," Opt. Express **27**(13), 17507–17520 (2019).
26. S. Ghanbari, K. A. Fedorova, A. B. Krysa, E. U. Rafailov, and A. Major, "Femtosecond Alexandrite laser passively mode-locked by an InP/InGaP quantum-dot saturable absorber," Opt. Lett. **43**(2), 232–234 (2018).
27. S. Ghanbari, R. Akbari, and A. Major, "Femtosecond Kerr-lens mode-locked Alexandrite laser," Opt. Express **24**(13), 14836–14840 (2016).
28. C. Cihan, A. Muti, I. Baylam, A. Kocabas, U. Demirbas, and A. Sennaroglu, "70 femtosecond Kerr-lens mode-locked multipass-cavity Alexandrite laser," Opt. Lett. **43**(6), 1315–1318 (2018).
29. C. Cihan, C. Kocabas, U. Demirbas, and A. Sennaroglu, "Graphene mode-locked femtosecond Alexandrite laser," Opt. Lett. **43**(16), 3969–3972 (2018).
30. T. H. Maiman, "Stimulated optical radiation in ruby," Nature **187**(4736), 493–494 (1960).
31. M. L. Shand, J. C. Walling, and R. C. Morris, "Excited-State Absorption in the Pump Region of Alexandrite," J. Appl. Phys. **52**(2), 953–955 (1981).
32. W. R. Kerridge-Johns and M. J. Damzen, "Analysis of pump excited state absorption and its impact on laser efficiency," Laser Phys. Lett. **12**(12), 125002 (2015).
33. W. R. Kerridge-Johns and M. J. Damzen, "Analytical model of tunable Alexandrite lasing under diode end-pumping with experimental comparison," J. Opt. Soc. Am. B **33**(12), 2525–2534 (2016).
34. P. Loiko and A. Major, "Dispersive properties of alexandrite and beryllium hexaaluminate crystals," Opt. Mater. Express **6**(7), 2177–2183 (2016).
35. P. Loiko, S. Ghanbari, V. Matrosov, K. Yumashev, and A. Major, "Dispersion and anisotropy of thermo-optical properties of Alexandrite laser crystal," Opt. Mater. Express **8**(10), 3000–3006 (2018).

Optical Materials EXPRESS

36. M. Pessot, J. Squier, G. Mourou, and D. J. Harter, "Chirped-Pulse Amplification of 100-Fsec Pulses," Opt. Lett. **14**(15), 797–799 (1989).
37. A. Hariharan, M. E. Fermann, M. L. Stock, D. J. Harter, and J. Squier, "Alexandrite-pumped alexandrite regenerative amplifier for femtosecond pulse amplification," Opt. Lett. **21**(2), 128–130 (1996).
38. M. L. Shand and H. P. Jenssen, "Temperature-Dependence of the Excited-State Absorption of Alexandrite," IEEE J. Quantum Electron. **19**(3), 480–484 (1983).
39. S. Guch and C. E. Jones, "Alexandrite-Laser Performance at High-Temperature," Opt. Lett. **7**(12), 608–610 (1982).
40. P. F. Moulton, "Spectroscopic and laser characteristics of Ti:Al_2O_3," J. Opt. Soc. Am. B **3**(1), 125–133 (1986).
41. D. Pugh-Thomas, B. M. Walsh, and M. C. Gupta, "Spectroscopy of BeAl2O4:Cr^{3+} with application to high-temperature sensing," Appl. Opt. **49**(15), 2891–2897 (2010).
42. M. L. Shand and J. C. Walling, "Excited-State Absorption in the Lasing Wavelength Region of Alexandrite," IEEE J. Quantum Electron. **18**(7), 1152–1155 (1982).
43. R. C. Powell, L. Xi, X. Gang, G. J. Quarles, and J. C. Walling, "Spectroscopic Properties of Alexandrite Crystals," Phys. Rev. B **32**(5), 2788–2797 (1985).
44. H. Ogilvy, M. J. Withford, R. P. Mildren, and J. A. Piper, "Investigation of the pump wavelength influence on pulsed laser pumped Alexandrite lasers," Appl. Phys. B: Lasers Opt. **81**(5), 637–644 (2005).
45. K. L. Schepler, "Fluorescence of Inversion Site Cr-$^{3+}$ Ions in Alexandrite," J. Appl. Phys. **56**(5), 1314–1318 (1984).
46. W. Gadomski and B. Ratajska-Gadomska, "Homoclinic orbits and chaos in the vibronic short-cavity standing-wave alexandrite laser," J. Opt. Soc. Am. B **17**(2), 188–197 (2000).
47. H. Burton, C. Debardelaben, W. Amir, and T. A. Planchon, "Temperature dependence of Ti:Sapphire fluorescence spectra for the design of cryogenic cooled Ti:Sapphire CPA laser," Opt. Express **25**(6), 6954–6962 (2017).
48. A. Bensalah, Y. Guyot, M. Ito, A. Brenier, H. Sato, T. Fukuda, and G. Boulon, "Growth of Yb^{3+}-doped YLiF4 laser crystal by the Czochralski method. Attempt of Yb^{3+} energy level assignment and estimation of the laser potentiality," Opt. Mater. **26**(4), 375–383 (2004).
49. U. Demirbas and I. Baali, "Power and efficiency scaling of diode pumped Cr: LiSAF lasers: 770–1110 nm tuning range and frequency doubling to 387–463 nm," Opt. Lett. **40**(20), 4615–4618 (2015).
50. L. G. DeShazer and K. W. Kangas, "Extended infared operation of titanium sapphire laser," *Conference on Lasers and Electro Optics* 14, 296–298 (1987).
51. U. Demirbas, R. Uecker, D. Klimm, and J. Wang, "Low-cost, broadly tunable (375-433 nm & 746-887 nm) Cr:LiCAF laser pumped by one single-spatial-mode diode," Appl. Opt. **51**(35), 8440–8448 (2012).
52. J. C. E. Coyle, A. J. Kemp, J. M. Hopkins, and A. A. Lagatsky, "Ultrafast diode-pumped Ti: sapphire laser with broad tunability," Opt. Express **26**(6), 6826–6832 (2018).
53. U. Demirbas, J. Wang, G. S. Petrich, S. Nabanja, J. R. Birge, L. A. Kolodziejski, F. X. Kartner, and J. G. Fujimoto, "100-nm tunable femtosecond Cr:LiSAF laser mode locked with a broadband saturable Bragg reflector," Appl. Opt. **56**(13), 3812–3816 (2017).
54. S. A. Payne, L. L. Chase, L. K. Smith, and B. H. T. Chai, "Flashlamp-Pumped Laser Performance of $LiCaAlF_6$ Cr^{3+}," Opt. Quantum Electron. **22**(S1), S259–S268 (1990).
55. S. A. Payne, L. L. Chase, L. K. Smith, W. L. Kway, and H. W. Newkirk, "Laser performance of $LiSAlF_6$:Cr^{3+}," J. Appl. Phys. **66**(3), 1051–1056 (1989).
56. D. E. McCumber, "Theory of phonon-terminated optical masers," Phys. Rev. **134**(2A), A299–A306 (1964).
57. M. L. Shand, "Quantum Efficiency of Alexandrite," J. Appl. Phys. **54**(5), 2602–2604 (1983).
58. Z. Y. Zhang, K. T. V. Grattan, and A. W. Palmer, "Thermal-Characteristics of Alexandrite Fluorescence Decay at High-Temperatures, Induced by a Visible Laser Diode Emission," J. Appl. Phys. **73**(7), 3493–3498 (1993).
59. R. Paschotta, *Encyclopedia of Laser Physics and Technology* (Wiley-VCH 2008).
60. M. Stalder, M. Bass, and B. H. T. Chai, "Thermal quenching of fluoresence in chromium-doped fluoride laser crystals," J. Opt. Soc. Am. B **9**(12), 2271–2273 (1992).
61. J. H. Wolter, M. A. Ahmed, and T. Graf, "Thin-disk laser operation of Ti:sapphire," Opt. Lett. **42**(8), 1624–1627 (2017).
62. U. Demirbas, A. Sennaroglu, F. X. Kartner, and J. G. Fujimoto, "Comparative investigation of diode pumping for continuous-wave and mode-locked Cr^{3+} : LiCAF lasers," J. Opt. Soc. Am. B **26**(1), 64–79 (2009).
63. R. Paschotta, *article on 'effective transition cross sections' in the Encyclopedia of Laser Physics and Technology* (Wiley-VCH 2008).
64. M. L. Shand, J. C. Walling, and H. P. Jenssen, "Ground-State Absorption in the Lasing Wavelength Region of Alexandrite - Theory and Experiment," IEEE J. Quantum Electron. **18**(2), 167–169 (1982).
65. W. Koechner, *Solid-state laser engineering* (Springer, New York, 2006).
66. A. Sennaroglu, *Photonics and Laser Engineering: Principles, Devices, and Applications* (McGraw-Hill Education, 2010).

88.255.99.18 {ts '2019-10-14 10:04:12'}